RSC Advances

PAPER

View Article Online
View Journal | View Issue

Cite this: *RSC Adv.*, 2022, **12**, 12136

Rational synthesis of IR820–albumin complex for NIR-II fluorescence imaging-guided surgical treatment of tumors and gastrointestinal obstruction†

Xinyu Feng,‡[a] Yuan Cao,‡[a] Pengrui Zhuang,[b] Ran Cheng,[a] Xuejun Zhang,[a] Hong Liu,*[c] Guohe Wang*[a] and Shao-Kai Sun *[a]

IR820, an analog of FDA-approved indocyanine green, is a promising second near-infrared window (NIR-II) fluorescence probe with better NIR-II fluorescence stability and great clinical transformation potential. Moreover, its fluorescence can be further remarkably enhanced by the interaction with albumin. Therefore, it is significant to flexibly design IR820–albumin complex using endogenous or exogenetic albumin to meet the requirements of different biological applications. Herein, we show the rational synthesis of IR820–albumin complex for NIR-II fluorescence imaging-guided surgical treatment of tumors and gastrointestinal obstruction. We compared the NIR-II fluorescence imaging ability of IR820 pre-incubated with albumin or not to visualize tumors and the gastrointestinal tract *in vivo* and found that the formation of IR820–albumin was essential for the intense NIR-II fluorescence. For imaging-guided tumor treatment, after intravenous injection of free IR820, IR820–albumin complex can be formed *in vivo* due to the presence of plenty of albumin in the blood. For imaging-guided gastrointestinal obstruction removal, IR820–albumin complex should be synthesized *in vitro* before oral administration. NIR-II fluorescence imaging-guided surgeries were successfully realized in both tumor resection and gastrointestinal obstruction removal. Besides, toxicity assessments *in vitro* and *in vivo* confirmed the good biocompatibility of IR820. Our study provides a flexible paradigm for IR820-based NIR-II fluorescence imaging and surgical navigation towards different diseases.

Received 21st January 2022
Accepted 30th March 2022

DOI: 10.1039/d2ra00449f

rsc.li/rsc-advances

Introduction

Surgical intervention plays an irreplaceable role in treating many diseases, such as cataracts, heart diseases, and malignant tumors.[1] Surgical operation guided by naked eye observation easily leads to many operative complications and residual lesions.[2,3] The emergence of imaging-guided surgical navigation greatly benefits improving the accuracy and safety of surgical operations.[4,5] Nowadays, several imaging approaches have been used in intraoperative navigation, such as fluorescence imaging, X-ray imaging, ultrasound imaging, magnetic resonance imaging, and computed tomography.[4–7]

Among various imaging methods, fluorescence imaging, which employs fluorescence probes to visualize the targets, possesses advantages of safety, real-time capability, high sensitivity, and portability.[8,9] In recent years, fluorescence imaging has been successfully applied in intraoperative real-time imaging for tumor resection and detection of lymph node metastasis in the clinic.[10–12] However, in practical applications, traditional fluorescence imaging still faces many limitations, like low tissue penetration depth, tissue autofluorescence, and fluorescence quenching.[13–16]

In recent years, second near-infrared window (NIR-II) fluorescence imaging (1000–1700 nm) has emerged as a new generation of upgraded fluorescence imaging.[17–19] Compared with visible and NIR-I (700–900 nm) fluorescence imaging, NIR-II fluorescence imaging exhibits higher resolution, deeper tissue penetration, smaller tissue autofluorescence, and lower optical scattering.[20,21] Currently, the developed NIR-II imaging probes mainly contain carbon nanotubes,[22] metal nanoclusters,[23–25] quantum dots,[26,27] rare earth chelates and nanoparticles,[28–38] conjugated polymers,[39,40] and small organic

[a]*School of Medical Imaging, Tianjin Medical University, Tianjin 300203, China. E-mail: wangguohe@tmu.edu.cn; shaokaisun@tmu.edu.cn*

[b]*Department of Radiology, The Second Hospital of Tianjin Medical University, Tianjin 300211, China*

[c]*The Second Surgical Department of Breast Cancer, Tianjin Medical University Cancer Institute and Hospital, National Clinical Research Center for Cancer, Key Laboratory of Cancer Prevention and Therapy, Tianjin's Clinical Research Center for Cancer, Tianjin 300060, China. E-mail: liuhongzhang0101@163.com*

† Electronic supplementary information (ESI) available: UV-vis-NIR absorption spectra, NIR-II fluorescence spectra, FT-IR spectra, Job's plots, modified Stern–Volmer plots, NIR-II fluorescence images, thermal stability studies, cytotoxicity studies. See https://doi.org/10.1039/d2ra00449f

‡ These authors contributed equally to the work.

dyes.[41–55] However, most of these probes are mainly studied in fundamental research, and there are still great challenges for their clinical transformation. Indocyanine green (ICG) is the only FDA-approved NIR fluorescence probe,[42] which is capable of NIR-II fluorescence imaging based on emission tails after 1000 nm.[56,57] ICG has been applied clinically for surgical resection of tumors and postoperative lymph node dissection,[10] but suffering from weak stability of fluorescent intensity.[58]

The cyanine dye IR820, an analog of ICG, has similar optical properties to ICG but better fluorescence stability.[58] IR820 and IR820-based nanomaterials have been used for NIR-II fluorescence imaging, photothermal therapy, and photodynamic therapy.[59–62] More importantly, intense fluorescence enhancement of IR820 can be achieved by forming IR820 and albumin complex.[59,60] The interaction between IR820 and the albumin can prevent IR820 molecules form aggregates in the aqueous solution, and reduce the aggregation-caused quenching effect. In addition, IR820 geometrical confinement by hydrophobic pockets of albumin could promote a rigid conformation, which minimizes the torsional rotations and weakens the non-radiative decay. The reasons above result in significantly increased fluorescence brightness of IR820 after binding with albumin.[59,63] This interesting effect facilitates the design of intraoperative imaging protocols for different administration routes. The commercial IR820 injected intravenously can directly covalently bind to serum albumin *in vivo* and has excellent photostability and bright fluorescence emission. This is a convenient and simple application method to reduce unnecessary synthesis steps. When administered orally, IR820–albumin complexes should be constructed *in vitro* to meet imaging needs due to insufficient albumin capable of fluorescence sensitization in the gastrointestinal tract. However, up to now, IR820-based imaging-guided surgery is limited to pre-synthesis of IR820–albumin *in vitro* for the following applications,[60] in which the design strategy can be improved by avoiding the unnecessary pre-synthesis process. Therefore, it is of great significance to rationally design IR820–albumin complex for NIR-II fluorescence imaging-guided surgical treatment with different administration routes.

Herein, we systematically study the design of IR820–albumin nanoprobes for NIR-II fluorescence imaging-guided surgical treatment with different administration routes. The free IR820 with good biocompatibility showed an NIR absorption peaked at 812 nm, and its fluorescence ranged from NIR-I to NIR-II regions. After incubation with albumin, the fluorescence of IR820 exhibited a remarkable enhancement due to the formation of the IR820–albumin complex. Based on the presence of plenty of albumins or not, the IR820–albumin complex was synthesized *in vivo* after intravenous injection of free IR820 and pre-synthesized *in vitro* before the oral administration, and the tumors and gastrointestinal tract can be seen clearly based on the NIR-II fluorescence imaging, respectively. Under the guidance of NIR-II fluorescence imaging, intraoperative navigation was achieved to relieve intestinal obstruction and resect tumors. The proposed protocol demonstrates IR820–albumin complex can be well employed for NIR-II fluorescence imaging-guided surgeries by various administration routes.

Experimental section

Materials

All chemicals were at least of analytical grade and used without further purification. IR820 dye and human serum albumin (HSA) were provided by Shanghai Macklin Biochemical Technology Co., Ltd. (Shanghai, China). Indocyanine green (ICG) was gained from Aladdin Reagent Co., Ltd. (Shanghai, China). Bovine serum albumin (BSA) was obtained from Beijing Dingguo Biotechnology Co., Ltd. (Beijing, China). Ultrapure water was bought from Wahaha Group Co., Ltd. (Hangzhou, China). DMSO was obtained from Concord Technology (Tianjin, China).

Characterization

The absorption spectra were recorded on a UV-3600 plus UV-Vis-NIR spectrophotometer (Shimadzu, Japan). The NIR-I and the NIR-II fluorescence emission spectra were measured on traditional (F7000, Hitachi, Japan) and NIR-II (NIRQuest512, Ocean Optics, USA) fluorescence spectrometers. Fourier transform infrared (FT-IR) spectra were characterized on a Nicolet iS10 spectrometer (Nicolet, USA). The NIR-II fluorescence imaging of IR820 and IR820–albumin *in vitro* and *in vivo* was carried out by a homemade small animal NIR-II imaging system. The excitation fluorescence was from a fiber coupling 808 nm laser system (Changchun New Industries Optoelectronics Technology Co., Ltd.). The absorbance for the MTT assay was determined with a microplate reader (Bio-tek, USA Park, CA).

Preparation of IR820–HSA

500 μM of IR820 and 500 μM HSA solutions were firstly prepared, and then 15 μL IR820, 30 μL HSA and 955 μL water were mixed and gently stirred at room temperature for 1 h. Then the IR820–HSA complex was generated and stored at 4 °C for later use.

Stability of IR820 and IR820–HSA complex

IR820–HSA complex was synthesized and dispersed in various media including water, PBS, and FBS for 48 h. The NIR-II fluorescence spectra of them were collected and the photo of each solution was taken to assess the optical and colloidal stability of the IR820–HSA complex. Besides, to evaluate the anti-photobleaching property, the IR820, IR820–HSA, ICG, ICG–HSA were exposed to continuous 808 nm illumination (120 mW cm^{-2}), and its fluorescence spectra were measured at various time points in 16 min.

To investigate the thermal stability, the IR820–HSA complex was heated and stirred in a water bath at different temperatures (25 °C, 40 °C, 50 °C, 60 °C, 70 °C, 80 °C) for 10 min, and the fluorescence intensity of IR820–HSA complex at different temperatures was determined.

Analysis of stoichiometric ratio

The classic Job's plot method was used to analyze the stoichiometric ratio of the reaction between IR820 and HSA. IR820 and HSA with different molar ratios were mixed, and the total

concentration of them was fixed to 8 μM. The UV-Vis-NIR absorption spectra of each solution were measured, and the absorbance at 835 nm was used to determine the stoichiometric ratio.

Determination of binding constant

For the fluorescence titration experiment, a fixed concentration (3 μM) of HSA in buffer solution (pH 2.4 for simulated gastric acid environment, pH 7.4 for physiological environment) was titrated with the gradual addition of IR820 (0, 1, 2, 3, 4, 5, 6 μM) at 298 K. The absorption and emission spectra (excited at 280 nm) of the solution were recorded. The binding constants were calculated by the Stern–Volmer equation using titration data.

Cytotoxicity evaluation

The cytotoxicity of IR820 and IR820–HSA was tested using a standard MTT assay. The mouse breast cancer cells (4T1 cells) and mouse embryonic fibroblasts (3T3-L1 cells) were seeded in 96-well plates (5×10^4 cells per well) and cultured in DMEM medium supplemented with 5% fetal bovine serum and 1% penicillin–streptomycin at 37 °C under the condition of 5% CO_2 for 12 h. The original media were discarded, and fresh media containing different concentrations of IR820 or IR820–HSA (0, 1, 2, 3, 4, 5, 6, 7, 8, 9 μM) were added to the cells and cultured for 24 h. After washing the cells with PBS, 10 μL MTT (5 mg mL^{-1}) and fresh media were added into each well and incubated for 4 h. Finally, 120 μL DMSO was added to each well of the plates to dissolve the purple formazan crystals, and the absorbance of each well at 490 nm was measured by a microplate reader.

Animal models

All animal procedures were performed in accordance with the guidelines of the Animal Care and Use Committee of Tianjin Medical University. All animal experiments were approved by the Animal Ethics Committee of Tianjin Medical University. Female Kunming mice and Balb/c mice were provided by Beijing HFK Bioscience Co., Ltd. (Beijing, China). To establish a 4T1-bearing model, 4T1 cells were injected subcutaneously on the back of Balb/c mice. The high intestinal obstruction model was built as follows. The skin and muscles of the abdomen were cut with forceps and surgical scissors to expose the duodenum carefully. Then, the duodenum was completely ligated with surgical sutures, and the wound was sutured cautiously.

In vivo NIR-II fluorescence imaging

All NIR-II fluorescence images were collected by a homemade small animal NIR-II imaging system. The imaging system mainly contained a thermoelectric cooled InGaAs camera (Princeton Instruments, NIRvana: 640, USA), a fiber-coupled 808 nm laser, and a 980 nm long-pass filter. Before imaging, all mice were anesthetized with the mixture of 0.5 L min^{-1} O_2 gas and 3% isoflurane in a small animal gas anesthesia machine, and all the imaging areas of mice were depilated. NIR-II fluorescence imaging of the gastrointestinal tract and high intestinal obstruction was carried out after the oral administration of IR820–HSA (400 μL, 7.5 μM). NIR-II fluorescence imaging of tumors in 4T1-bearing mice was performed with the tail vein injection of free IR820 (150 μL, 75 μM). Three mice were used in each group. Different camera exposure times and excitation power density were used to collect fluorescence images of the digestive tract system (1000 ms, 58 mW cm^{-2}) and tumors (200 ms, 116 mW cm^{-2}). Finally, the images were analyzed by ImageJ software.

Histopathological analysis

Kunming mice were treated with tail vein injection of 150 μL, 75 μM IR820 or oral administration of 400 μL, 7.5 μM IR820–HSA. The mice treated with the same volume of PBS (10 mM, pH 7.4) were set as the control groups. The mice were sacrificed on day 1, day 7, and day 14 after injection, and the main organs (including heart, liver, spleen, lung, kidney and digestive tract) were acquired. After that, the tissues were fixed in 4% formaldehyde solution for hematoxylin-eosin (H&E) staining.

Results and discussion

Preparation and characterization of the IR820 and IR820–albumin

We first measured the absorption and NIR-II fluorescence spectra of IR820. IR820 has strong absorption in the NIR-I region, and the two absorption peaks were located at 685 nm and 812 nm (Fig. S1a†). Upon the excitation of an 808 nm laser, an NIR-II fluorescence tail emission wavelength could reach about 1200 nm (Fig. S1b†). IR820 showed the highest fluorescence intensity at the concentration of 7.5 μM both in ultrapure water and PBS, and the fluorescence intensity of IR820 in ultrapure water was higher than that in PBS at any concentrations (Fig. S1c†).

To further enhance the NIR-II fluorescence, IR820–HSA was fabricated by the simple mixture of IR820 and HSA solutions

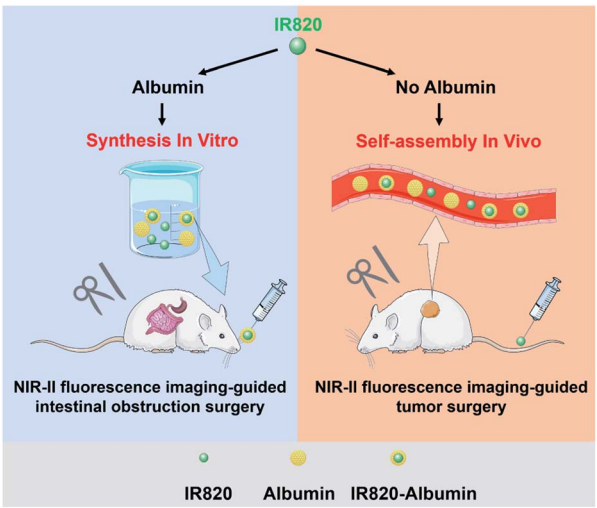

Scheme 1 Schematic diagram of the construction of IR820–albumin complex and NIR-II fluorescence imaging-guided surgery of intestinal obstruction and tumors.

(Scheme 1). FT-IR spectra of IR820–HSA showed characteristic bands for S=O stretching vibration (1273 cm^{-1}), Amide I (1649 cm^{-1}) and Amide II (1535 cm^{-1}),[64,65] revealing the presence of IR820 and HSA (Fig. S2†). UV-Vis-NIR absorption spectra were used to investigate the interaction between HSA and IR820. The maximum absorption peak of IR820–HSA has a significant redshift from 685 nm to 835 nm (Fig. 1a), indicating the strong interaction between IR820 and HSA. Absorption Job's plot at different pHs (pH 2.4 for simulated gastric acid environment, pH 7.4 for physiological environment) showed a 3 : 2 stoichiometric ratio of IR820 to HSA (approach to 1 : 1) according to the absorption at 835 nm of IR820–HSA (Fig. S3†).[66] In addition, a fluorescence titration experiment was performed by gradually adding IR820 into HSA to quench the fluorescence of HSA at 330 nm. The calculated binding constants determined by the Stern–Volmer equation were all above 1×10^5 L mol^{-1}, which indicated that IR820 had an excellent affinity to HSA under acidic and physiological conditions (Fig. S4†). Then the fluorescence enhancement effect of HSA on IR820 was studied. The concentration of IR820 was maintained at 7.5 μM, and different concentrations of HSA were added. When the molar ratio of IR820 to HSA was 1 : 2, strong fluorescence enhancement could be observed, and a 13.2-fold fluorescent increase was achieved at 1000 nm (Fig. 1b). As the HSA content further increased (no higher than 5 mg mL^{-1}), the fluorescence increase degree tended to be flat (Fig. S5†). Therefore, the molar ratio of IR820 to HSA was determined to 1 : 2 as the optimum reaction condition, which could ensure that nearly all of IR820 was complexed to HSA. Besides, the obvious fluorescence enhancement and redshift in absorption spectra were both observed at different pHs due to the formation of the stable IR820–HSA complex. Especially, IR820–HSA showed stronger absorption and fluorescence in an acidic environment, benefiting the application of IR820–HSA in the acidic gastrointestinal environment (Fig. S6†).

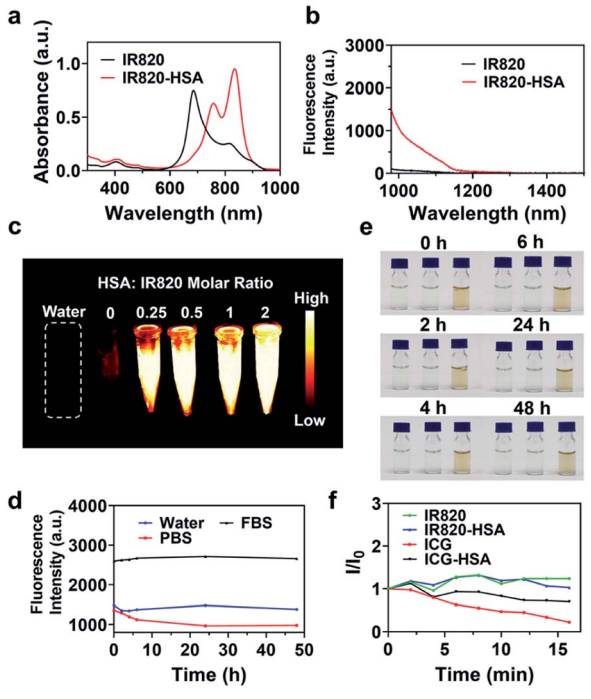

Fig. 1 Characterization of IR820 and IR820–HSA. (a) UV-Vis-NIR absorbance spectra of IR820 and IR820–HSA. (b) Fluorescence spectra of IR820 and IR820–HSA under the excitation of an 808 nm laser. (c) NIR-II images of IR820–HSA with different content of HSA. (d) The fluorescence intensity stability of IR820–HSA in water, PBS, and FBS in 48 h. (e) Colloid stability of IR820–HSA in water, PBS, and FBS in 48 h (from left to right). (f) Photobleaching curves of IR820, IR820–HSA, ICG, ICG–HSA exposed to continuous irradiation at 808 nm for 16 min (120 mW cm^{-2}).

Then we investigated the NIR-II fluorescence imaging ability of IR820 and IR820–HSA complex *in vitro*. Upon the irradiation of 808 nm laser, an intense NIR-II fluorescence of IR820–HSA can be observed clearly, and the fluorescent intensity increased with the molar ratio of HSA to IR820 (Fig. 1c). It should be noted that the fluorescent intensity was much higher than that of free IR820 due to the powerful sensitization effect of HSA towards IR820. These results indicated the formation of IR820–HSA is essential to obtain superior NIR-II imaging performance.

We then compared the fluorescence intensity of IR820 with ICG in the presence of albumin or not. The NIR-II fluorescence intensity of free IR820 was lower than that of ICG (Fig. S7a†). After dissolved in 1 mg mL^{-1} HSA (molar ratio of ICG to HSA, 1 : 2), the fluorescence intensity of the formed IR820–albumin complex was comparable to that of ICG–albumin (Fig. S7a†). However, in the presence of high concentrations of albumins, such as mouse serum, FBS, and high concentrations of BSA and HSA with the equivalent concentration of albumin in serum (40 mg mL^{-1}), the NIR-II fluorescence intensity of the generated IR820–albumin complex became much higher than that of ICG–albumin (Fig. S7b†). The NIR-II fluorescence images of IR820 and ICG in the presence of albumin or not also showed similar results (Fig. S7c†). These results demonstrated IR820 exhibited great potential in NIR-II fluorescence imaging by intravenous injection due to the formation of IR820–albumin with superior fluorescence.

To investigate the stability of IR820–HSA, the IR820–HSA complex was synthesized and dispersed in various media for 48 h, and the fluorescence intensity and the solution status were monitored at different time points (Fig. 1d and e). The results indicated the NIR-II fluorescence of each solution all kept stable, and there was no visible aggregate in 48 h, which indicated the good optical and colloidal stability of the IR820–HSA complex. To examine the anti-photobleaching ability, IR820 and IR820–HSA complex were exposed to a continuous 808 nm laser irradiation. The fluorescence of IR820 and IR820–HSA both showed a neglectable decrease, which revealed IR820 and IR820–HSA owned excellent anti-photobleaching ability. In contrast, the fluorescence of ICG and ICG–HSA declined obviously under the same condition (Fig. 1f). Besides, the thermal stability was also evaluated by heating the IR820–HSA at different temperatures for 10 min. The results indicated that the fluorescence intensity of IR820–HSA didn't change much until the reaction temperature rose to 80 °C due to its excellent thermal stability (Fig. S8†). These studies showed the synthesized IR820–HSA complex exhibited favorable optical, colloidal, and thermal stability.

Cytotoxicity assessment of IR820 and IR820–HSA

Standard MTT analysis was used to test the cytotoxicity of IR820 and IR820–HSA. To study the potential cytotoxicity of IR820 and IR820–HSA, 3T3-L1 cells and 4T1 cells were exposed to various concentrations of IR820 and IR820–HSA after 24 h incubation, respectively. When the concentration was 9 μM, the cell viability of the two cells was still higher than 80% (Fig. S9†). These results indicated good biocompatibility of IR820 and IR820–HSA.

In vivo NIR-II fluorescence imaging of gastrointestinal tract

Given the above-mentioned excellent NIR-II fluorescence imaging properties of IR820 and IR820–HSA, we investigated the feasibility of imaging ability of digestive tract diseases using IR820 and IR820–albumin. Kunming mice ($n = 3$) were orally administrated with IR820–HSA (400 μL, 7.5 μM), and fluorescence images were collected by an InGaAs camera (exposure time, 1000 ms) irradiated upon an 808 nm laser excitation (58 mW cm^{-2}). As shown in Fig. 2a, a bright fluorescence signal could be quickly observed in the stomach after oral administration at 1 min. When the time was extended to 6 h, strong fluorescence was obtained in the small intestine. The fluorescence signal greatly reduced at 24 h, and became neglectable at 48 h. In order to further understand the excretion of IR820–HSA in mice, we carried out fluorescence imaging of the main organs of mice at different time points after oral administration *ex vivo* and determined their fluorescence signal intensity (Fig. 2b and c). These results confirmed that IR820–HSA was mainly excreted through the digestive tract from the body after 48 h, instead of accumulated *in vivo*. At the same time, we imaged the mice with free IR820 by intragastric administration under the same conditions and monitored the excretion process of IR820 in the digestive tract (Fig. S10†). The entire excretion process was as same as that of IR820–HSA, but the fluorescence signal of free IR820 was not enough to brighten the digestive tract very well. According to the results, due to the insufficient albumin in the gastrointestinal tract, IR820–HSA should be pre-synthesized for high-performance NIR-II fluorescence imaging, which showed great potential in the real-time diagnosis of gastrointestinal diseases.

Diagnosis of intestinal obstruction and NIR-II imaging-guided intestinal obstruction surgery

To further explore the application of IR820–HSA in digestive diseases, we established the mouse model of high intestinal obstruction. The mice were orally administered with IR820–HSA (400 μL, 7.5 μM), and NIR-II fluorescence images were recorded at different time points (0 min, 10 min, 20 min, and 30 min) (Fig. 3a). After oral injection of IR820–HSA, the stomach was full of the imaging probes with a strong fluorescent signal, which kept constant in at least 30 min, indicating that the IR820–HSA solution remained in the stomach and couldn't be excreted. Imaging of the digestive tract of mice with high intestinal obstruction *ex vivo* also showed IR820–HSA with intense fluorescent signal was blocked in the stomach (Fig. 3b). As a result, the location of obstruction could be observed, which makes imaging-guided surgery possible. Then we operated under the imaging guidance of IR820–HSA, and the entire surgery process was recorded (Fig. 3c and Video S1†). Thanks to the excellent imaging ability of IR820–HSA with a high signal-to-noise ratio, intestinal obstruction removal could be achieved in an ultra-simple and fast way. After surgery to relieve the obstruction, IR820–HSA passed through the obstructive area and was

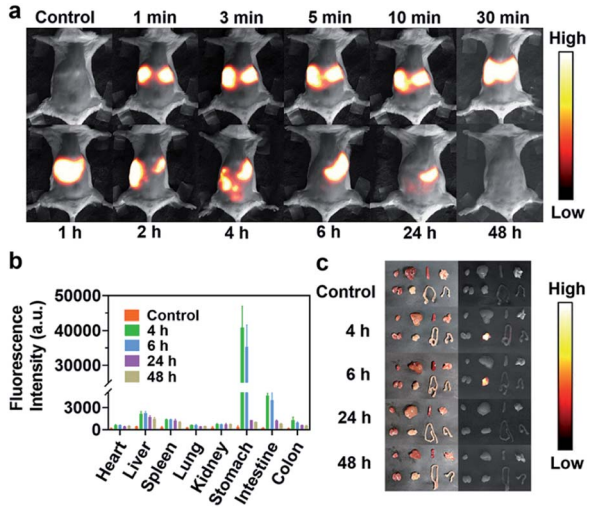

Fig. 2 NIR-II fluorescence imaging of digestive tract. (a) The NIR-II fluorescence images of the digestive tract after oral administration of IR820–HSA at different time points (1000 ms, 58 mW cm^{-2}). (b) The average signal of major organs at different time points after oral administration of IR820–HSA (means ± SD, $n = 3$). (c) *Ex vivo* fluorescence imaging of major organs harvested from mice treated with IR820–HSA at different time points.

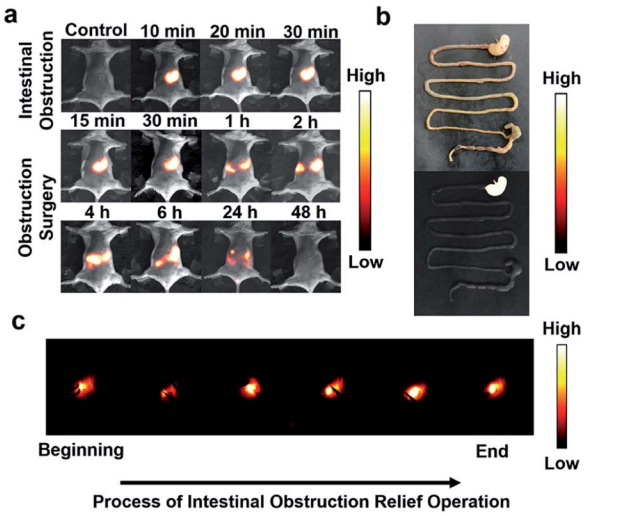

Fig. 3 NIR-II fluorescence imaging of intestinal obstruction. (a) NIR-II fluorescence imaging of intestinal obstruction before and after obstruction surgery. (b) *Ex vivo* NIR-II fluorescence images of intestinal obstruction after administration of IR820–HSA at 30 min. (c) Video captures of NIR-II fluorescence imaging-guided relief of intestinal obstruction.

excreted from the body within 48 h (Fig. 3a). The above results indicated that IR820–HSA could be applied to diagnose and guide intestinal obstruction surgery with great potential clinical value.

In vivo NIR-II imaging of tumors

We then evaluated the feasibility of NIR-II fluorescence imaging of tumors *in vivo* using IR820–albumin complex. Considering the high content of albumin in blood, IR820–albumin complex can be formed *in vivo* by intravenous injection of free IR820 in theory. So 4T1 tumor-bearing Balb/c mice ($n = 3$) were injected with IR820 (150 μL, 75 μM) *via* the tail vein, and NIR-II fluorescence images of mice were collected at different time points (0, 4, 24, 48, 72, 96 h) (Fig. 4a). At 4 h after administration, intense NIR-II fluorescence of IR820 was observed in the whole body. At longer time points, the location and boundary of the tumor gradually became clearer based on the enhanced permeability and retention effect. The tumor-to-background (T/B) ratios was analyzed ($n = 3$) (Fig. 4b). At 48 h, the T/B ratio reached the highest value of 5.5, which reflected the excellent NIR-II imaging properties of IR820 in mice. To investigate the detailed biodistribution of IR820 in the body better, tumors and main organs were dissected at different time points after the administration of free IR820 ($n = 3$), and *ex vivo* imaging was performed. Bright fluorescence was observed in tumors, kidneys and livers, which indicated the fluorescence probe was mainly drained out of the body through the digestive and urinary systems (Fig. 4c and d). As time went by, the fluorescence signal intensity in livers and other major organs gradually reduced, while that in tumors first increased and finally decreased, which was similar to imaging *in vivo*. To prove that IR820 can be self-assembled with albumins to form an enhanced fluorescent complex *in vivo*, we performed the tumor imaging of mice after being injected with IR820–HSA at the same condition (150 μL, 75 μM) through the tail vein (Fig. S11a†). The maximum T/B ratio was 5 at 48 h (Fig. S11b†). The results indicated there was no obvious difference in fluorescence imaging performance of tumors with IR820–HSA and IR820 since IR820–albumin can be formed *in vivo*. The above studies demonstrated IR820–albumin complex formed *in vivo* can serve as an excellent NIR-II fluorescence imaging probe for delineation of tumor boundary and potential imaging-guided tumor resection.

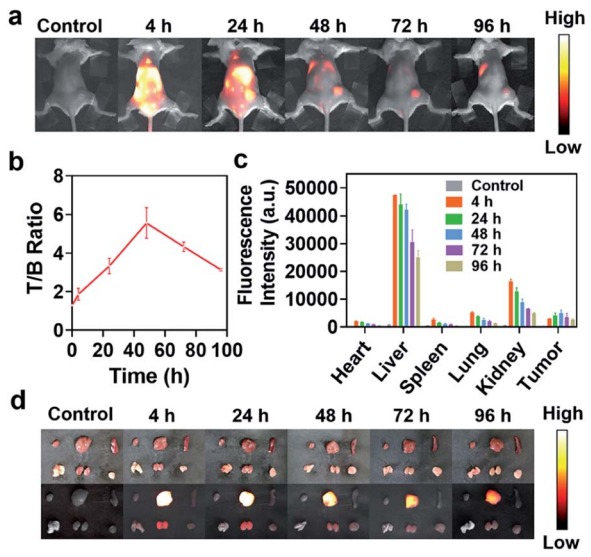

Fig. 4 NIR-II fluorescence imaging of tumors. (a) NIR-II fluorescence images of tumor mice injected with free IR820 at different time points. (b) Tumor-to-background ratios curve at different time points (means ± SD, $n = 3$). (c) Average signals from major organs and tumors at different time points after injection of IR820 (means ± SD, $n = 3$). (d) *Ex vivo* NIR-II fluorescence images of tumors and major organs after IR820 administration.

NIR-II fluorescence imaging-guided tumor resection

After the intravenous injection of IR820, the tumor-bearing Balb/c mice were subjected to real-time precise tumor resection under intraoperative NIR-II fluorescence imaging (Fig. 5 and Video S2†). First, NIR-II imaging was used to locate the tumor accurately, then the tumor was carefully separated from the surrounding tissues and removed. Under the real-time visualized NIR-II imaging, the tumor was completely resected, and there was no residual tumor tissue. These results demonstrated IR820–albumin complex generated *in vivo* can be used as a powerful NIR-II fluorescence imaging probe for the real-time imaging-guided complete tumor resection.

Histopathological analysis

To evaluate the *in vivo* toxicity of IR820–albumin complex, the mice were treated with tail vein injection of free IR820 (150 μL, 75 μM) or oral administration of IR820–HSA complex (400 μL, 7.5 μM), and the histopathological analysis of the main organs was completed at different time points. No significant histopathological damage of the major organs, including hearts, livers, spleens, lungs, kidneys and digestive tracts, was observed in all of the mice with different treatments (Fig. 6a and b). The results demonstrated that the IR820–albumin complex possesses good biosafety for biological applications *in vivo*.

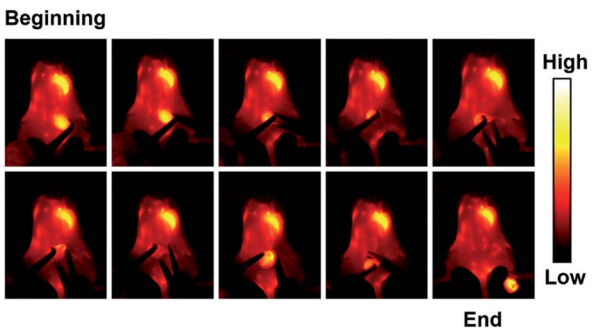

Fig. 5 Images of the intraoperative NIR-II fluorescence imaging-guided tumor resection.

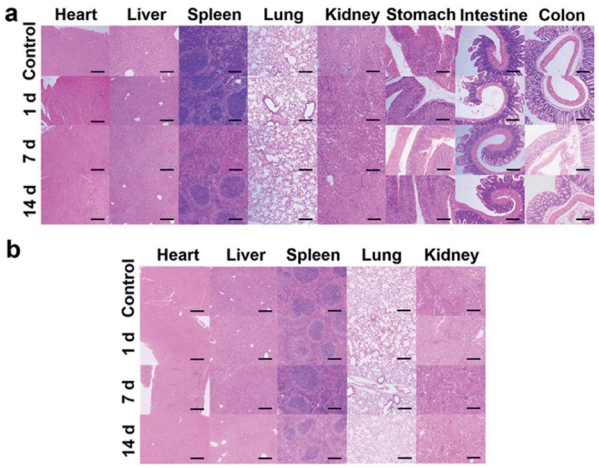

Fig. 6 H&E stained images of (a) major organs (heart, lung, liver, spleen, kidney, stomach, intestine, and colon) by orally injected and (b) major organs (heart, lung, liver, spleen, kidney, and tumor) by injected through the tail vein.

Conclusions

In summary, based on superior NIR-II fluorescence features of IR820 and fluorescence sensitization effect of albumin, a protocol adapted to different administration routes of NIR-II fluorescence imaging and surgical navigation is proposed. This flexible design contains the spontaneous formation of the IR820–albumin complex after intravenous administration due to the high concentration of albumin in the blood and the pre-synthesis of the IR820–HSA complex *in vitro* necessary for oral administration. The bright NIR-II fluorescence signal and good biosafety of IR820–albumin complex have been studied, and real-time NIR-II fluorescence imaging of the gastrointestinal system and tumors were successfully realized. Moreover, accurate intestinal obstruction relief and tumor resection can be achieved under the guidance of intraoperative NIR-II imaging with IR820–albumin. Therefore, IR820–albumin complex shows a bright prospect in NIR-II imaging-guided surgeries for different diseases with great clinical transformation potential. Furthermore, the proposed flexible strategy provides a universal protocol for biological applications of NIR-II fluorescent dyes.

Author contributions

X. F. and Y. C. contributed equally to this work. All authors have given approval to the final version of the manuscript.

Conflicts of interest

The authors declare no competing financial interest.

Acknowledgements

This work was supported by financial support from the National Natural Science Foundation of China (21874101, 21934002, 82071982, and 81801770) and the Natural Science Foundation of Tianjin City (19JCJQJC63700 and 19JCQNJC11100).

References

1 R. Sullivan, O. I. Alatise, B. O. Anderson, R. Audisio, P. Autier, A. Aggarwal, C. Balch, M. F. Brennan, A. Dare, A. D'Cruz, A. M. M. Eggermont, K. Fleming, S. M. Gueye, L. Hagander, C. A. Herrera, H. Holmer, A. M. Ilbawi, A. Jarnheimer, J.-f. Ji, T. P. Kingham, J. Liberman, A. J. M. Leather, J. G. Meara, S. Mukhopadhyay, S. S. Murthy, S. Omar, G. P. Parham, C. S. Pramesh, R. Riviello, D. Rodin, L. Santini, S. V. Shrikhande, M. Shrime, R. Thomas, A. T. Tsunoda, C. van de Velde, U. Veronesi, D. K. Vijaykumar, D. Watters, S. Wang, Y.-L. Wu, M. Zeiton and A. Purushotham, *Lancet Oncol.*, 2015, **16**, 1193–1224.
2 T. E. Bertrand, A. Cruz, O. Binitie, D. Cheong and G. D. Letson, *Clin. Orthop. Relat. Res.*, 2016, **474**, 677–683.
3 E. L. Vos, J. Gaal, C. Verhoef, K. Brouwer, C. H. M. van Deurzen and L. B. Koppert, *Eur. J. Surg. Oncol.*, 2017, **43**, 1846–1854.
4 C. Chi, Y. Du, J. Ye, D. Kou, J. Qiu, J. Wang, J. Tian and X. Chen, *Theranostics*, 2014, **4**, 1072–1084.
5 U. Mezger, C. Jendrewski and M. Bartels, *Langenbeck's Arch. Surg.*, 2013, **398**, 501–514.
6 C. Wang, Z. Wang, T. Zhao, Y. Li, G. Huang, B. D. Sumer and J. Gao, *Biomaterials*, 2018, **157**, 62–75.
7 P. L. Kubben, K. J. ter Meulen, O. E. M. G. Schijns, M. P. ter Laak-Poort, J. J. van Overbeeke and H. v. Santbrink, *Lancet Oncol.*, 2011, **12**, 1062–1070.
8 Z. Guo, S. Park, J. Yoon and I. Shin, *Chem. Soc. Rev.*, 2014, **43**, 16–29.
9 M. Gao, F. Yu, C. Lv, J. Choo and L. Chen, *Chem. Soc. Rev.*, 2017, **46**, 2237–2271.
10 Z. Hu, C. Fang, B. Li, Z. Zhang, C. Cao, M. Cai, S. Su, X. Sun, X. Shi, C. Li, T. Zhou, Y. Zhang, C. Chi, P. He, X. Xia, Y. Chen, S. S. Gambhir, Z. Cheng and J. Tian, *Nat. Biomed. Eng.*, 2020, **4**, 259–271.
11 S. Hernot, L. van Manen, P. Debie, J. S. D. Mieog and A. L. Vahrmeijer, *Lancet Oncol.*, 2019, **20**, e354–e367.
12 S. Hameed and Z. Dai, *Mater. Today Chem.*, 2018, **10**, 90–103.
13 C. Li, G. Chen, Y. Zhang, F. Wu and Q. Wang, *J. Am. Chem. Soc.*, 2020, **142**, 14789–14804.
14 F. Ding, Y. Fan, Y. Sun and F. Zhang, *Adv. Healthcare Mater.*, 2019, **8**, e1900260.
15 C. Li and Q. Wang, *ACS Nano*, 2018, **12**, 9654–9659.
16 Kenry, Y. Duan and B. Liu, *Adv. Mater.*, 2018, **30**, e1802394.
17 M. Kamimura, *Anal. Sci.*, 2021, **37**, 691–697.
18 H. Wan, H. Du, F. Wang and H. Dai, *Adv. Funct. Mater.*, 2019, **29**, 1900566.
19 G. Hong, A. L. Antaris and H. Dai, *Nat. Biomed. Eng.*, 2017, **1**, 0010.
20 R. Q. Yang, K. L. Lou, P. Y. Wang, Y. Y. Gao, Y. Q. Zhang, M. Chen, W. H. Huang and G. J. Zhang, *Small Methods*, 2021, **5**, 2001066.

21 F. Ding, Y. Zhan, X. Lu and Y. Sun, *Chem. Sci.*, 2018, **9**, 4370–4380.
22 G. Hong, S. Diao, J. Chang, A. L. Antaris, C. Chen, B. Zhang, S. Zhao, D. N. Atochin, P. L. Huang, K. I. Andreasson, C. J. Kuo and H. Dai, *Nat. Photonics*, 2014, **8**, 723–730.
23 W. Wang, Y. Kong, J. Jiang, Q. Xie, Y. Huang, G. Li, D. Wu, H. Zheng, M. Gao, S. Xu, Y. Pan, W. Li, R. Ma, M. X. Wu, X. Li, H. Zuilhof, X. Cai and R. Li, *Angew. Chem., Int. Ed.*, 2020, **59**, 22431–22435.
24 X. Song, W. Zhu, X. Ge, R. Li, S. Li, X. Chen, J. Song, J. Xie, X. Chen and H. Yang, *Angew. Chem., Int. Ed.*, 2020, **60**, 1306–1312.
25 H. L. Liu, G. S. Hong, Z. T. Luo, J. C. Chen, J. L. Chang, M. Gong, H. He, J. Yang, X. Yuan, L. L. Li, X. Y. Mu, J. Y. Wang, W. B. Mi, J. Luo, J. P. Xie and X. D. Zhang, *Adv. Mater.*, 2019, **31**, 1901015.
26 Z.-Y. Liu, A.-A. Liu, H. Fu, Q.-Y. Cheng, M.-Y. Zhang, M.-M. Pan, L.-P. Liu, M.-Y. Luo, B. Tang, W. Zhao, J. Kong, X. Shao and D.-W. Pang, *J. Am. Chem. Soc.*, 2021, **143**, 12867–12877.
27 C. Li, W. Li, H. Liu, Y. Zhang, G. Chen, Z. Li and Q. Wang, *Angew. Chem., Int. Ed.*, 2020, **59**, 247–252.
28 P. Zhuang, K. Xiang, X. Meng, G. Wang, Z. Li, Y. Lu, D. Kan, X. Zhang and S. K. Sun, *J. Mater. Chem. B*, 2021, **9**, 2285–2294.
29 Z. B. Qu, J. L. Shen, Q. Li, F. Xu, F. Wang, X. L. Zhang and C. H. Fan, *Theranostics*, 2020, **10**, 2631–2644.
30 L. Ma, S. Huang, S. He, Z. Wang and Z. Cheng, *Biosens. Bioelectron.*, 2020, **151**, 112000.
31 J. T. Xu, A. Gulzar, P. P. Yang, H. T. Bi, D. Yang, S. L. Gai, F. He, J. Lin, B. G. Xing and D. Y. Jin, *Coord. Chem. Rev.*, 2019, **381**, 104–134.
32 P. Wang, Y. Fan, L. Lu, L. Liu, L. Fan, M. Zhao, Y. Xie, C. Xu and F. Zhang, *Nat. Commun.*, 2018, **9**, 2898.
33 M. Zhang, Z. Wang, C. Wang, Y. Wu, Z. Li and Z. Liu, *ACS Nano*, 2021, **15**, 11940–11952.
34 J. T. Xu, R. P. Shi, G. Y. Chen, S. M. Dong, P. P. Yang, Z. Y. Zhang, N. Niu, S. L. Gai, F. He, Y. J. Fu and J. Lin, *ACS Nano*, 2020, **14**, 9613–9625.
35 C. Wang, H. Lin, X. Ge, J. Mu, L. Su, X. Zhang, M. Niu, H. Yang and J. Song, *Adv. Funct. Mater.*, 2020, **31**, 2009942.
36 Y. Zhong, Z. Ma, F. Wang, X. Wang, Y. Yang, Y. Liu, X. Zhao, J. Li, H. Du, M. Zhang, Q. Cui, S. Zhu, Q. Sun, H. Wan, Y. Tian, Q. Liu, W. Wang, K. C. Garcia and H. Dai, *Nat. Biotechnol.*, 2019, **37**, 1322–1331.
37 S. F. Wang, L. Liu, Y. Fan, A. M. El-Toni, M. S. Alhoshan, D. D. Li and F. Zhang, *Nano Lett.*, 2019, **19**, 2418–2427.
38 Y. Li, S. Zeng and J. Hao, *ACS Nano*, 2019, **13**, 248–259.
39 Z. Zhang, X. Fang, Z. Liu, H. Liu, D. Chen, S. He, J. Zheng, B. Yang, W. Qin, X. Zhang and C. Wu, *Angew. Chem., Int. Ed.*, 2020, **59**, 3691–3698.
40 S. Wang, J. Liu, G. Feng, L. G. Ng and B. Liu, *Adv. Funct. Mater.*, 2019, **29**, 1808365.
41 L. Zhang, X. Shi, Y. Li, X. Duan, Z. Zhang, H. Fu, X. Yang, J. Tian, Z. Hu and M. Cui, *J. Med. Chem.*, 2021, **64**, 7735–7745.
42 Z. Lei and F. Zhang, *Angew. Chem., Int. Ed. Engl.*, 2021, **60**, 16294–16308.
43 S. Wang, B. Li and F. Zhang, *ACS Cent. Sci.*, 2020, **6**, 1302–1316.
44 Y. Li, Y. F. Liu, Q. Q. Li, X. D. Zeng, T. Tian, W. Y. Zhou, Y. Cui, X. K. Wang, X. D. Cheng, Q. H. Ding, X. F. Wang, J. Z. Wu, H. Deng, Y. Q. Li, X. L. Meng, Z. X. Deng, X. C. Hong and Y. L. Xiao, *Chem. Sci.*, 2020, **11**, 2621–2626.
45 S. J. Zhu, R. Tian, A. L. Antaris, X. Y. Chen and H. J. Dai, *Adv. Mater.*, 2019, **31**, 1900321.
46 S. He, J. Song, J. Qu and Z. Cheng, *Chem. Soc. Rev.*, 2018, **47**, 4258–4278.
47 B. Li, M. Zhao, L. Feng, C. Dou, S. Ding, G. Zhou, L. Lu, H. Zhang, F. Chen, X. Li, G. Li, S. Zhao, C. Jiang, Y. Wang, D. Zhao, Y. Cheng and F. Zhang, *Nat. Commun.*, 2020, **11**, 3102.
48 Y. Fang, J. Shang, D. Liu, W. Shi, X. Li and H. Ma, *J. Am. Chem. Soc.*, 2020, **142**, 15271–15275.
49 S. Wang, Y. Fan, D. Li, C. Sun, Z. Lei, L. Lu, T. Wang and F. Zhang, *Nat. Commun.*, 2019, **10**, 1058.
50 R. Tian, Q. Zeng, S. Zhu, J. Lau, S. Chandra, R. Ertsey, K. S. Hettie, T. Teraphongphom, Z. Hu, G. Niu, D. O. Kiesewetter, H. Sun, X. Zhang, A. L. Antaris, B. R. Brooks and X. Chen, *Sci. Adv.*, 2019, **5**, eaaw0672.
51 W. Feng, Y. Zhang, Z. Li, S. Zhai, W. Lv and Z. Liu, *Anal. Chem.*, 2019, **91**, 15757–15762.
52 B. Li, L. Lu, M. Zhao, Z. Lei and F. Zhang, *Angew. Chem., Int. Ed.*, 2018, **57**, 7483–7487.
53 A. L. Antaris, H. Chen, S. Diao, Z. R. Ma, Z. Zhang, S. J. Zhu, J. Wang, A. X. Lozano, Q. L. Fan, L. L. Chew, M. Zhu, K. Cheng, X. C. Hong, H. J. Dai and Z. Cheng, *Nat. Commun.*, 2017, **8**, 15269.
54 X. D. Zhang, H. S. Wang, A. L. Antaris, L. L. Li, S. Diao, R. Ma, A. Nguyen, G. S. Hong, Z. R. Ma, J. Wang, S. J. Zhu, J. M. Castellano, T. Wyss-Coray, Y. Y. Liang, J. Luo and H. J. Dai, *Adv. Mater.*, 2016, **28**, 6872–6879.
55 A. L. Antaris, H. Chen, K. Cheng, Y. Sun, G. Hong, C. Qu, S. Diao, Z. Deng, X. Hu, B. Zhang, X. Zhang, O. K. Yaghi, Z. R. Alamparambil, X. Hong, Z. Cheng and H. Dai, *Nat. Mater.*, 2016, **15**, 235–242.
56 S. Zhu, B. C. Yung, S. Chandra, G. Niu, A. L. Antaris and X. Chen, *Theranostics*, 2018, **8**, 4141–4151.
57 S. Zhu, Z. Hu, R. Tian, B. C. Yung, Q. Yang, S. Zhao, D. O. Kiesewetter, G. Niu, H. Sun, A. L. Antaris and X. Chen, *Adv. Mater.*, 2018, **30**, e1802546.
58 A. Fernandez-Fernandez, R. Manchanda, T. Lei, D. A. Carvajal, Y. Tang, S. Z. R. Kazmi and A. J. McGoron, *Mol. Imaging*, 2012, **11**, 99–113.
59 Z. Feng, X. Yu, M. Jiang, L. Zhu, Y. Zhang, W. Yang, W. Xi, G. Li and J. Qian, *Theranostics*, 2019, **9**, 5706–5719.
60 B. Du, C. Qu, K. Qian, Y. Ren, Y. Li, X. Cui, S. He, Y. Wu, T. Ko, R. Liu, X. Li, Y. Li and Z. Cheng, *Adv. Opt. Mater.*, 2019, **8**, 1901471.
61 X. Hu, H. Tian, W. Jiang, A. Song, Z. Li and Y. Luan, *Small*, 2018, **14**, e1802994.
62 W. Li, J. Peng, L. Tan, J. Wu, K. Shi, Y. Qu, X. Wei and Z. Qian, *Biomaterials*, 2016, **106**, 119–133.

63 A. L. Antaris, H. Chen, S. Diao, Z. Ma, Z. Zhang, S. Zhu, J. Wang, A. X. Lozano, Q. Fan, L. Chew, M. Zhu, K. Cheng, X. Hong, H. Dai and Z. Cheng, *Nat. Commun.*, 2017, **8**, 15269.
64 T. Dymerski, J. Namieśnik, H. Leontowicz, M. Leontowicz, K. Vearasilp, A. L. Martinez-Ayala, G. A. González-Aguilar, M. Robles-Sánchez and S. Gorinstein, *Food Res. Int.*, 2016, **83**, 74–86.
65 X. He, J. Hong, S. Liu, D. Xu and H. Hu, *Carbohydr. Res.*, 2021, **508**, 108416.
66 I. M. Khan, S. Shakya, R. Akhtar, K. Alam, M. Islam and N. Alam, *Bioorg. Chem.*, 2020, **100**, 103872.